Sectional Lift Coefficient of a Rotating wing at Low Reynolds Number

Jieun Kim
School of Mechanical and Aerospace Engineering
Seoul National University

Abstract

To investigate the characteristics of sectional lift coefficient, we conduct three-dimensional simulations of flow around a low-aspect-ratio wing in rotating motion at a low Reynolds number (Re=136). Three different shapes of flat plate wings (fruit-fly, rectangular, and triangular wings) are considered but keeping their aspect ratio (wing span/wing chord) the same at 3.74. Each wing rotates at a constant angular velocity and the angle of attack (AoA) is fixed during the rotation. During the first rotation, the sectional lift coefficient decreases from the wing root to the wing tip for all cases. After a few rotations, the wing is exposed to the downward motion generated from the previous rotation and thus the sectional lift coefficient is overall reduced. The effect of wing shape on the sectional lift coefficient are explored with three different types of thin plate wings. We also investigate the behavior of sectional lift coefficient at higher Reynolds number.

Keywords: sectional lift coefficient, rotating wing, low-aspect-ratio wing, wing shape

Student number: 2011-22885

Contents

List of Figures

Nomenclature

Roman Symbols

AR	wing aspect ratio
b	wing span length
c	wing chord length
c_{2D}	wing chord length of 2D wing
$\bar{c}$	mean chord length ($=S/b$)
C_D	drag coefficient
C_L	lift coefficient
C_p	pressure coefficient
D	drag
$\mathbf{f}$	momentum forcing
L	lift
L_{2D}	lift on 2D wing
O	rotation center
p	pressure
q	mass source/sink
r_0	spanwise (radial) position of wing root
r_{tip}	spanwise (radial) position of wing tip
r^*	non-dimensional spanwise (radial) position ($=r/r_{tip}$)
R	rotational matrix
Re	Reynolds number
S	wing planform area
t	time

T	rotational period
$\mathbf{u}$	velocity vector in inertial reference frame
$\mathbf{u}_r$	velocity vector in non-inertial reference frame
U	reference velocity
U_r	maximum transitional velocity of wing element
$\mathbf{x}$	orthogonal coordinates in inertial reference frame (x, y, z)
$\mathbf{x}_r$	orthogonal coordinates in non-inertial reference frame (x_r, y_r, z_r)

Greek Symbols

α	angle of attack
α_{eff}	effective angle of attack
ϕ	rotation angle
$\dot{\phi}$	rotation angular velocity
Γ	circulation of vortex
ν	kinematic viscosity
ρ	density
ω_r	radial vorticity

Abbreviations

AOA	angle of attack
LEV	leading-edge vortex
WTV	wing-tip vortex

Chapter 1

Introduction

Aerodynamic research on micro-air-vehicles (MAV) has been gaining significant interest from the research community over the past few years. MAV has evolved into various types such as fixed wing, rotary wing, and flapping wing. Fixed wing type MAV is best developed type of MAVs and exhibits quite good forward flight capabilities. Recently, flapping wing type MAV such as orhnithoper and entomopter is of increasing concern motivated by elevated aerodynamic performance of birds and insect flights. Nevertheless, rotary wing type MAV is the only configurations capable to combine acceptable high and low speed characteristics including hovering, and it is also the only controllably hovering flying objects at the moment.

To design a MAV, the first consideration is the amount of lift force generated from the wing, which should be large enough to support the weight of MAV. For the rotary wing, the blade element theory (BET) has been used to estimate the lift force generation. In the theory, the lift force is obtained by breaking down a wing blade into several elements, determining the forces on each wing element, and integrating them along the entire wing. One of the most important components for the theory is to know the radial distribution of the sectional lift coefficient. The sectional lift coefficient ($C_{L,S}$) on each wing element (Δr) is defined as

$$C_{L,S}(r,t) = \frac{\Delta L(r,t)}{0.5\rho U_r^2(r)c(r)\Delta r} \tag{1.1}$$

where ΔL is the sectional lift force, r is the spanwise (or radial) direction, t is the time, ρ is the density, U_r is the maximum translational velocity of the wing element, and c is the chord length, respectively.

For high-aspect-ratio wing at low angle of attack and high Reynolds number, the sectional lift coefficient has been assumed to be constant in radial direction based on the potential theory because the sectional lift force of the wing element is proportional to where is the circulation around the wing element. This assumption has been proven to be valid for relatively low aspect ratio wings (AR=6-10) in rotating motion at high Reynolds number (Caradonna & Tung (1981); Morino *et al.* (1989)).

During the last decade, the vortical structures around low-aspect-ratio wing in rotating motion at low Reynolds number have been investigated to understand the force generation mechanism of insect flight. Elevated aerodynamic performance of insect flight has been identified to be related to generation and maintenance of leading-edge vortex (LEV) in rotating motion, thus the vortical structures have been observed to explain the stability of the LEV. Lentink & Dickinson (2009) performed experiments to determine the important parameters governing the LEV attachment using a dynamically scaled robot model of a fruit fly wing. Their flow visualization indicated that the LEV is stabilized by the quasi-steady centripetal and Coriolis accelerations and resulted from the rotating motion of the wing. Kim & Gharib (2010) observed flow structures of low-aspect-ratio (AR=2.3) wing in translational and rotational motion. Their results supported the concept that the spanwise flow is responsible for prolonging the attachment of the LEV to the wing for the rotating motion as compared to pure translation. Devoria *et al.* (2011) performed dye flow visualization and DPIV with rotating low-aspect-ratio (AR=2, 4) rectangular plates as a simplified models of a hovering-wing in order to understand the effect of the significant root-to-tip flow on the vortex formation. Ozen & Rockwell (2012) experimentally observed that a stable LEV on the low-aspect-ratio rotating wing is maintained over AoA from 30° to 75°.

From the above studies, further understanding of the flow structures around the rotating wing has been made, but much attention has not been paid to the sectional lift coefficient. Luo & Sun (2005) showed that the hawkmoth and dragonfly wings in rotating motion have constant $C_{L,S}$ up to 50% and 70% of wing span, respectively. On the other hand, Poelma *et al.* (2006) showed by applying Kutta-Joukowski theorem that $C_{L,S}$ is constant initially and is proportional to $1/r$ in quasi-steady state up to 80% of wing span for rotating drosophila wing.

For the flight of flapping wing in hovering motion, recent direct measurements of the sectional lift coefficient have shown that $C_{L,S}$ is inversely proportional to the radial position r up to 70% of the wing span (Birch *et al.* (2004); Nagai & Hayase (2009)). Especially, Kweon & Choi (2010) from their numerical simulations showed that the time-averaged $C_{L,S}$ varies in inverse proportion to radial position except very near the wing tip and the sectional lift coefficient on the flapping wing is significantly affected by the flows generated from the previous strokes.

As shown above, the controversy about radial distribution of the sectional lift coefficient has remained unresolved and when the blade element theory is applied, and the conventional assumption of constant $C_{L,S}$ may not be appropriate to low-aspect-ratio wing in rotating motion at low Reynolds number. Hence, the information on the variation of the instantaneous sectional lift coefficient of rotating wing is required to determine the relation of $C_{L,S} \sim r^n$ in order to estimate its lift forces. In addition, one of the most important features for stable hovering flight is the lift force generation in steady state. Nonetheless, the above studies on aerodynamics of the rotating wing cannot deal with the rotating flight in steady state due to the small rotation angle considered ($\leq 180°$).

In the present study, we conduct numerical simulations of flow around the low-aspect-ratio wing in rotating motion to investigate the characteristics of sectional lift coefficient. The temporal characteristics of the sectional lift coefficient is examined from the impulsive start to steady state at various angles of attack. We explore the wing shape effects for the three different types of thin plate wings and address the Reynolds number dependency of sectional lift coefficient. Also, the vortical structures around the rotating wing are investigated to explain the characteristics of the sectional lift coefficient. Finally, the sectional lift coefficient is compared to the lift coefficient of two-dimensional wing at the same Reynolds number to evaluate the possibility of sectional lift coefficient estimation of three-dimensional wing using the result of two-dimensional simulations.

Chapter 2

Numerical Details

Figure 2.1(a) shows three types of wing planforms considered in the present study: fruit-fly, rectangular and triangular wings. The shape of fruit fly wing is the same as that of mechanical model of robotic fly by Dickinson *et al.* (1999). Aspect ratio (AR) of the wings, which is defined as the square of the wingspan b divided by the wing planform area S, is maintained as 3.74 corresponding to the fruit-fly wing and the wing thickness is set as $0.05\bar{c}$, where $\bar{c}(= S/b)$ is the mean chord length. The distance between the wing root and rotation center is $0.73\bar{c}$. The wing impulsively starts to rotate from rest and the rotational angular velocity is determined as 0.2237 to match the wing-tip velocity as 1. Angle of attack (AoA) of the wing is fixed throughout the rotations.

The Reynolds number considered is Re=U$\bar{c}/\nu$=136 (if not mentioned otherwise), corresponding to that of the flapping fruit-fly wing in hovering flight, based on the tip velocity U and mean chord length (Dickinson *et al.* (1999)). We conduct additional simulations at higher Re (=500) in order to investigate the behavior of sectional lift coefficient at higher Re.

Three-dimensional flow around a rotating wing is simulated with an immersed boundary method in a non-inertial reference frame proposed by Kim & Choi (2006). No-slip boundary condition at the moving body surface is satisfied by including momentum forcing and mass source/sink to the Navier-Stokes and continuity equations, respectively. In a non-inertial reference frame, simulation of a moving body requires much less grid points than in an inertial reference frame. The governing equations in the non-inertial reference frame are given as

$$\frac{\partial \mathbf{u}_n}{\partial t} + \nabla \cdot [(\mathbf{u}_n - \mathbf{v})\mathbf{u}_n + \mathbf{u}_n\mathbf{w}] = -\nabla p + \frac{1}{Re}\nabla^2 \mathbf{u}_n + \mathbf{f} \tag{2.1}$$

$$\nabla \cdot \mathbf{u}_n - q = 0 \tag{2.2}$$

where $\mathbf{u}_n = \mathbf{u}_r + \mathbf{v} = \mathbf{R}^\mathbf{T}\mathbf{u}$, $\mathbf{v} = \Omega \times \mathbf{u}_r + \mathbf{u}_s$, $\mathbf{w} = \Omega \times \mathbf{x}_r$, p is the pressure, $\mathbf{f}$ is the momentum forcing, and q is the mass source/sink. $\mathbf{x}_r$ and $\mathbf{u}_r$ are the orthogonal coordinates and corresponding velocity vector in the non-inertial reference frame, respectively. $\mathbf{u}$ is the velocity vector in the inertial reference frame, $\mathbf{R}$ is the rotation matrix, and $\mathbf{u}_s$ and Ω are the translational and angular velocities in the non-inertial reference frame, respectively. How to determine $\mathbf{R}$, $\mathbf{f}$ and q for flow around a moving body is described in detail in Kim & Choi (2006).

Figure 2.1(b) shows the wing shape and coordinate system and the size of the computational domain is -20 $< x_r/\bar{c} <$ 25, -20 $< y_r/\bar{c} <$ 20, and -20 $< z_r/\bar{c} <$ 20. Dirichlet boundary conditions ($\mathbf{u}_r$=0) are applied at all outer boundaries. The number of grid points is 257×161×193 at Re=136, 385×225×257 at Re=500 and in x_r, y_r, and z_r directions, respectively, with the smallest resolution of $\Delta z_{r,min} = 0.01\bar{c}$ to resolve the wing thickness.

In order to validate the code, we conduct a three-dimensional simulation of rotating wing and compare the results with the previous study (Lan & Sun (2001)). The Reynolds number is set equal to 156 and the wing AoA is 35°. Figure 2.2 shows lift coefficient (C_L) and drag coefficient (C_D) behavior of low-aspect-ratio wing (AR=2) in rotational motion with constant angular velocity after an initial acceleration motion from rest. Here, the lift coefficient and the drag coefficient are defined as $C_L = L/0.5\rho U^2 S$ and $C_D = D/0.5\rho U^2 S$. The present result agrees well with the reference data after the initial acceleration period (maximum error$< 2\%$ at $t > 1$). Discrepancies in magnitude of C_L and C_D peaks at the initial acceleration have no significant influence on the analysis of present study.

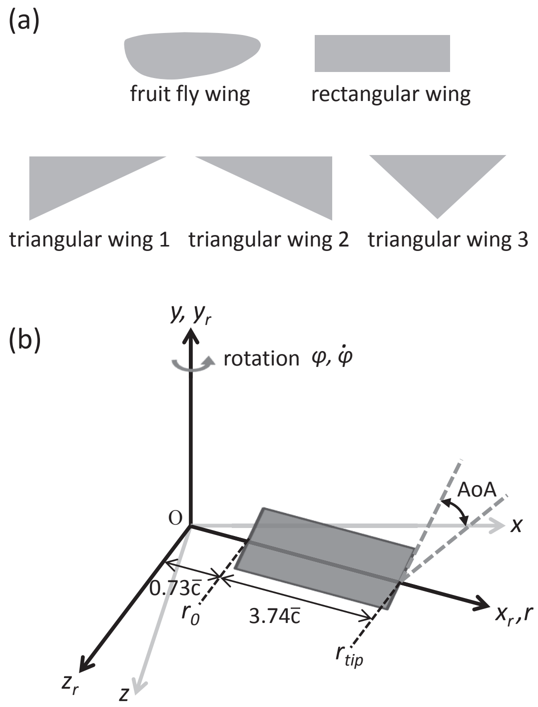

Figure 2.1. (a) Wing shapes; (b) Wing body and coordinates: (x, y, z) in an inertial reference frame and (x_r, y_r, z_r) in a non-inertial reference frame fixed to the wing body.

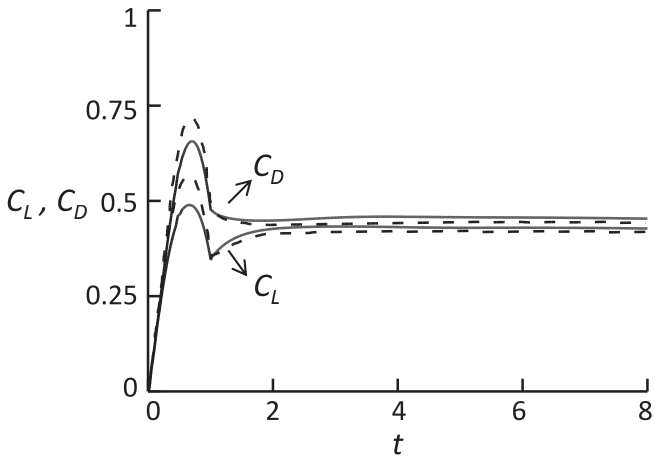

Figure 2.2. Temporal variation of the lift and drag coefficient: (solid line) present study; (dashed line) Lan and Sun (2001).

Chapter 3

Numerical Results

3.1 Temporal behavior of lift coefficient

The wing impulsively starts to rotate from rest in still air and after one rotational period (T), the wing is influenced by the flows generated from the previous rotation. The simulations are conducted for 6-7 rotations until the force generation is observed to be in steady state. Figure 3.1 shows the temporal behaviors of lift coefficient at different AoAs of the wings, where the lift coefficient is defined as $C_L = L/0.5\rho U^2 S$. During the first rotation, C_L is almost constant at $t/T \leq 0.9$ because the leading edge vortex (LEV) generated by rotational motion is attached while the LEV sheds from the wing in translational motion. At the end of the first rotation, C_L drops rapidly near $t/T \sim 1$ due to the reduction of effective AoA by encountering the downwash flows induced from the previous rotation. The drop rate of lift coefficient is about 30%. Figure 3.2 shows sectional velocity vector fields and spanwise vorticity contours at $r^* = 0.5$. At higher AoA, larger LEV is attached on the wing leading-edge and it induces stronger downwash flows behind the rotating wing, resulting in abrupt drop of lift force near the end of the first rotation. The wings experience another drop in the lift at $2 \leq t/T \leq 2.5$, and thereafter C_L shows gradual decrease (AoA=5° and 15°) or oscillatory behavior (AoA=30° and 45°). After four rotations ($t/T \geq 4$), C_L becomes almost steady.

3.2 Spanwise distribution of instantaneous sectional lift coefficient

Figure 3.3(a) shows the spanwise distribution of instantaneous sectional lift coefficient at t/T=0.6. During the most of the first rotation period ($0.3 < t/T < 0.9$), the spanwise distribution of instantaneous $C_{L,S}$ is almost identical (not shown here). At this period, $C_{L,S}$ decreases from the wing root to the wing tip, and its gradient in the radial direction becomes steeper at higher AoA. Lentink *et al.* (2009) measured the three-dimensional flow around an auto-rotating maple seed which operates at high AoA ($30° - 60°$). They showed that decreasing sectional lift coefficient behavior of auto-rotating seed which is similar to our results.

We obtain the relation $C_{L,S} \sim r^{*m}$ from the instantaneous $C_{L,S}$ on the midsection of the wing ($20\% - 70\%$ of the wing span) where the LEV is attached and plot the distribution of exponent m at various AoAs in Figure 3.3(c). The exponent m decreases from -0.5 to -1 with increasing AoA ($\leq 40°$) and it stays roughly constant (around -1) at broad range of AoA ($40° - 80°$) varying about ± 0.1. The relation $C_{L,S} \sim 1/r^*$ at high AoA is consistent with the previous observation of Poelma *et al.* (2006), which showed that the sectional circulation on the wing-mid section of rotating wing is almost constant at rotation angle $\phi \geq 90°$. Figure 3.3(d) reveals that sectional circulation is nearly constant over the wing-mid section at various high AoAs ($= 40°, 50°, 60°, 70°$). This supports the variation of exponent m at high AoA in Figure 3.3(c) and also indicates that the Kutta-Joukowski hypothesis is partly applicable to predict the distribution of lift force from the rotating wing at high AoA. The sharp reduction at $r^* > 0.6$ occurs due to the wing-tip vortex.

As described before, C_L becomes steady after about four rotations. Figure 3.3(b) shows the spanwise distribution of instantaneous sectional lift coefficient at the steady state (t/T=4.6). $C_{L,S}$ is overall reduced due to downwash flows generated from the previous rotations and becomes a steady state, similar to rotary wing in hovering. At low AoA ($\leq 15°$), $C_{L,S}$ becomes nearly constant except near the wing root and tip. On the other hands, at high AoA ($= 30°$ and $45°$), $C_{L,S}$ maintains the behavior similar to that of first rotation but its gradient in the radial direction becomes less steep. As shown in Figure 3.3(c), m exhibits a gross increase from the initial to steady state. At high AoA ($\geq 55°$), the exponent is slightly larger than -1, which was observed from the previous numerical (Nagai & Hayase (2009); Kweon & Choi (2010)) and experimental studies (Birch *et al.* (2004)) on the flapping wing in hovering motion.

Figure 3.4(a) and (b) show sectional velocity fields at r^*=0.5 at AoA=45°. Unlike the first rotation, downwash motion is observed in front of the rotating wing in the sectional velocity fields after several rotations. To quantify the effect of downwash flows from previous rotations, we examine the effective AoA of the rotating wing. The effective AoA is defined as shown in Figure 3.4(c) and is obtained by averaging velocity vectors within the shaded region in Figure 3.4(a) and (b). Figure 3.4(d) shows the spanwise distribution of effective AoA for the rectangular wing at AoA= 45°. After several rotations, the effective AoA shows a considerable decrease overall and the reduction is more significant near the wing root (-25%). This observation supports the substantial reduction of sectional lift coefficient near the wing root.

3.3 Wing shape effect on sectional lift coefficient

In regard to the MAV design, one of the most important components is to determine the wing shape. To investigate the wing shape effect on the sectional lift coefficient, the results from three different types of wing planforms are illustrated in Figure 3.5. As shown in Figure 3.5(a), the lift coefficients of triangular wings exhibit high dependency on the wing shape and show different temporal behaviors during rotations. Among the triangular wings, it is appeared that the wing having large chord length near the wing-tip generates more lift force because its LEV induces lower pressure on broader region of the wing suction surface (Figure 3.6). The maximum spanwise vorticity magnitude of LEV of triangular wing 2 is larger than that of triangular wing 1 about 17%, 20%, 37% at r^{*}=0.3, 0.5, 0.8, respectively. On the other hand, the spanwise distributions of sectional lift coefficient are quite similar regardless of wing planforms, as shown in Figure 3.5(b) and (c). The results of triangular wings are a little bit scattered but they show similar tendency, especially near the wing tip where the translational velocity is relatively larger.

3.4 The behavior of sectional lift coefficient at higher Reynolds number

To investigate the behavior of $C_{L,S}$ at higher Reynolds number, we conduct additional simulations of flows around rotating rectangular wing at higher Re (=500). Figure 3.7(a), (b) shows spanwise distribution of instantaneous $C_{L,S}$ depending on Re. At low AoA (=5°), $C_{L,S}$ at high Re shows quite similar behavior with the results at Re=136, exhibiting slight discrepancies. At high AoA (=45°), however, $C_{L,S}$ at higher Re is much larger than that of Re=136 near the wing root (region A), but similar near the wing tip (region B). As described before, $C_{L,S}$ distribution at Re=136 is overall reduced after several rotations ($t/T = 4.6$). On the other hand, $C_{L,S}$ of higher Re shows large reduction near the wing root (region A) and it keeps similar behavior near the wing tip (region B). Figure 3.8(b) shows instantaneous vertical velocity field on the stroke plane of the rotating rectangular wing at AoA=45° during the first rotation at Re=500. Strong downward flow is mainly observed behind the region A of the wing and it is induced by leading-edge vortex (LEV), wing-root vortex (WRV) and wing-tip vortex (WTV) as shown in Figure 3.8(a). The downward flow suppresses LEV and it leads to reduction of $C_{L,S}$ in region A after several rotations. In region B, complex behavior of WTVs prevents strong downward flow and it results in maintenance of $C_{L,S}$ behavior near the wing tip (region B).

3.5 The possibility of sectional lift coefficient estimation of 3D wing

When we adopt the blade element theory to estimate the lift force of rotating wing, complex behaviors of sectional lift coefficient are observed due to three-dimensional effect of the wing such as wing-tip vortex and wing-root vortex. A series of 2D simulations are conducted to evaluate the possibility of $C_{L,S}$ estimation of 3D wing using the result of 2D simulations. The rectangular wing whose aspect ratio is 4 is considered at Re=100 in 3D simulations with the angle of attack 5°, 15°, 30°, 45°. In 2D simulations, the rectangular wing whose thickness is same as 3D wing is considered like the cross-section of 3D wing and the 2D wing motion is obtained by projecting the motion of 3D wing element to 2D plane. Eight elements of the 3D wing are chosen for 2D simulations and the distance between the wing element and the rotation center varies from $1.0c_{2D}$ to $4.5c_{2D}$ in increment of $0.5c_{2D}$. According to the spanwise location of the corresponding 3D wing element, Re of 2D wing increases from 20 to 90, respectively. 225×193 ($x \times y$) grid points are used in the domain $-2 < x/c_{2D} <$

6, $-4 < y/c_{2D} < 4$, and the minimum grid size is $0.01c_{2D}$. To realize the wing shape, an immersed boundary method in an inertial reference frame (Kim & Choi (2001)) is used. The lift coefficient of 2D wing is defined as

$$C_{L,S} = \frac{L_{2D}}{0.5\rho U^2 c_{2D}}$$

where L_{2D} is the lift force on the 2D wing.

Figure 3.9 shows the variations of the sectional lift coefficient of 3D rotating wing and the lift coefficient of 2D translating wing. The lift coefficient of 2D wing is almost same regardless of the Reynolds number, as it has been reported in previous studies. As angle of attack is higher, there is a distinct difference in results between 2D simulation and 3D simulation. Hence, we cannot estimate the behavior of the sectional lift coefficient with 2D simulations due to the 3D effects.

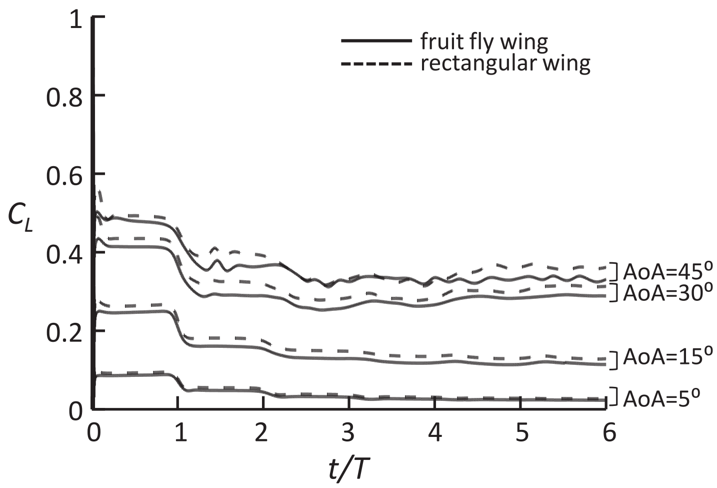

Figure 3.1. Temporal behavior of the lift coefficient (C_L); T is the rotational period.

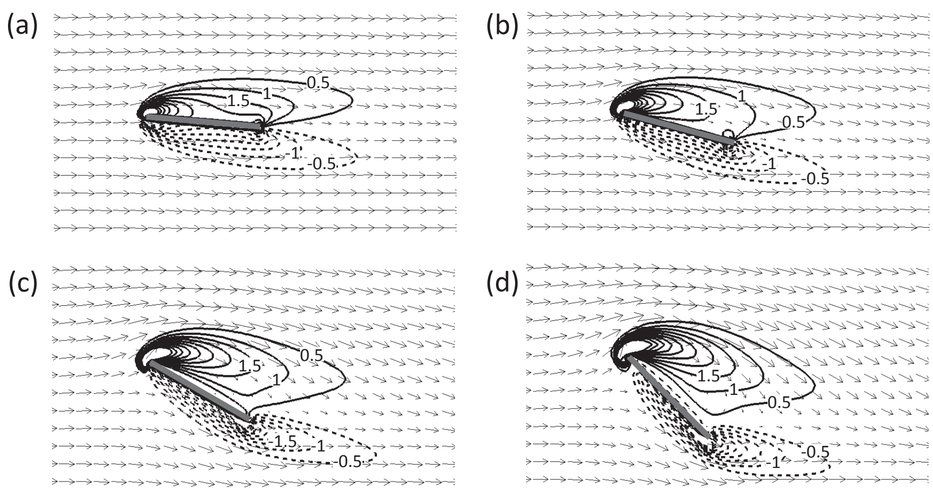

Figure 3.2. Sectional velocity vector fields as arrows $(u_r - U_r, u_y)$ and spanwise vorticity (ω_r) contour at r^*=0.5; In this representation, we subtract the maximum translational velocity of the wing element U_r from each spanwise velocity vector u_r in order to observe downward flow. All sectional velocity vector fields in this study are represented through the same calculation. (a) AoA=5° (b) AoA=15° (c) AoA=30° (d) AoA=45°.

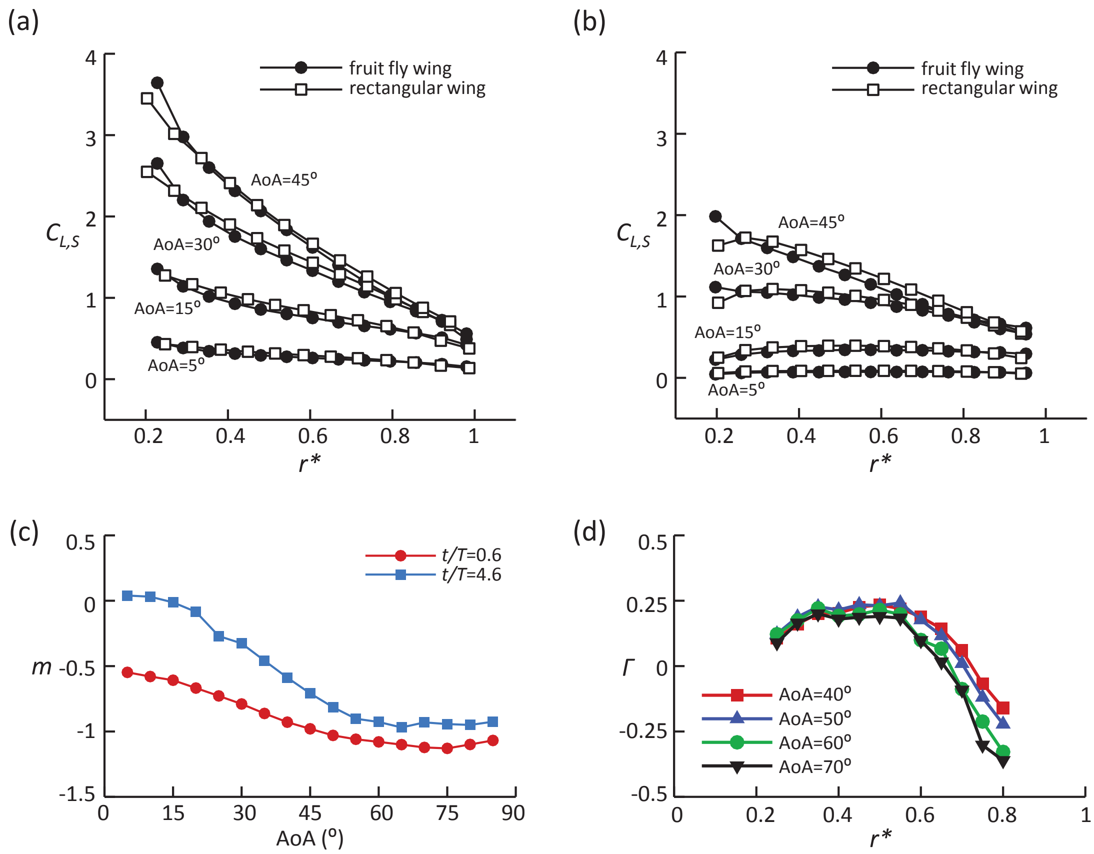

Figure 3.3. Spanwise distribution of instantaneous sectional lift coefficient at (a) t/T=0.6 (b) t/T=4.6: Here, $r^* = r/r_{tip}$ (c) m obtained from relationship $C_{L,S} \sim r^{*m}$ with rectangular wing at various AoAs ($5^\circ - 85^\circ$). (d) Sectional circulation of rotating rectangular wing in spanwise direction at AoA=$40^\circ - 70^\circ$. In (d), the circulations (Γ) are computed at each spanwise location by integrating the spanwise vorticity (ω_r) over areas encircled by 5% of $|\,\omega_r\,|_{max}$.

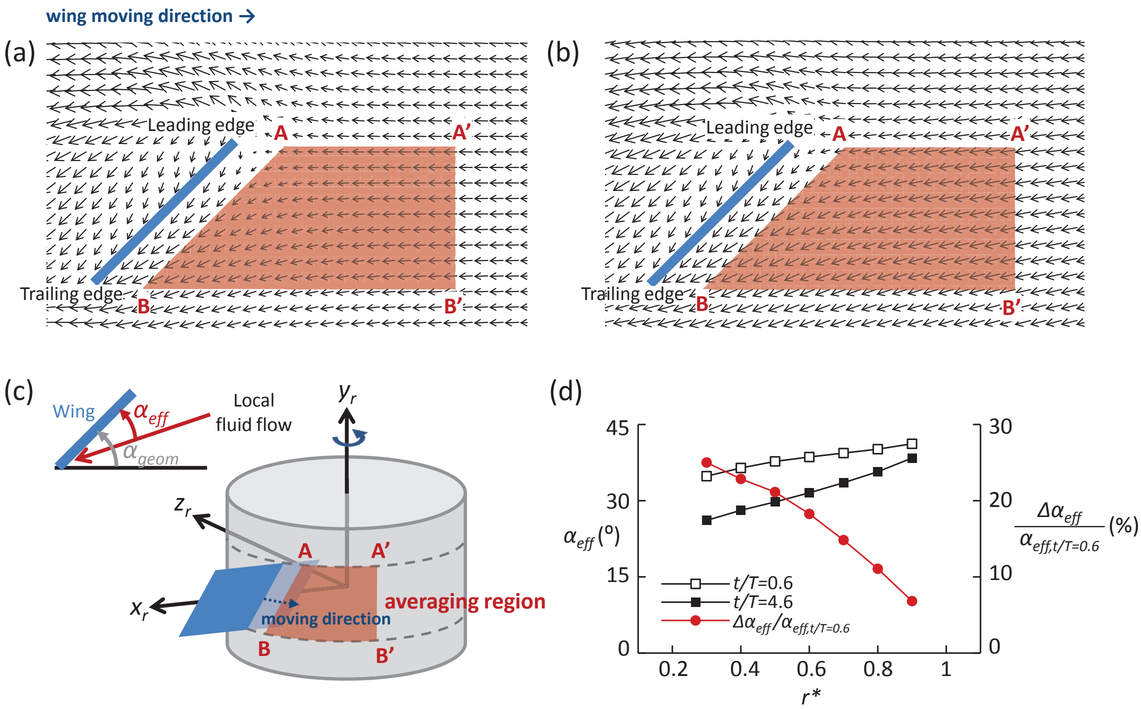

Figure 3.4. Sectional velocity vector fields of rectangular wing at AoA=45° as arrows ($u_r - U_r$,u_y) at r^*=0.5, (a) t/T=0.6 (b) t/T=4.6 (c) Definition of effective angle of attack (α_{eff}) and schematic diagram of averaging region of velocity vectors (d) Spanwise distributions of effective angle of attack (α_{eff}) and its percentage of reduction: Here, $\Delta\alpha_{eff}$=$\alpha_{eff,t/T=0.6} - \alpha_{eff,t/T=4.6}$.

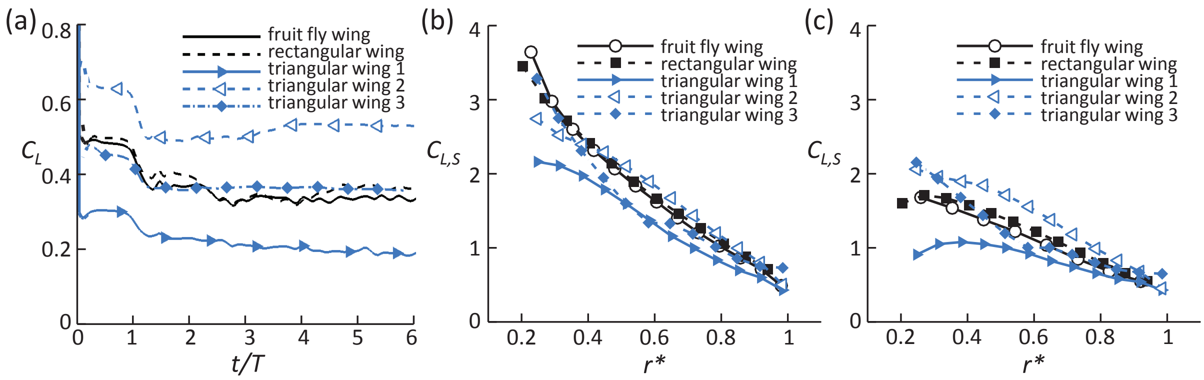

Figure 3.5. (a) Temporal lift coefficient behaviors of five different planform wings. Spanwise distribution of instantaneous sectional lift coefficient with the wings at (b) t/T=0.6 (c) t/T=4.6.

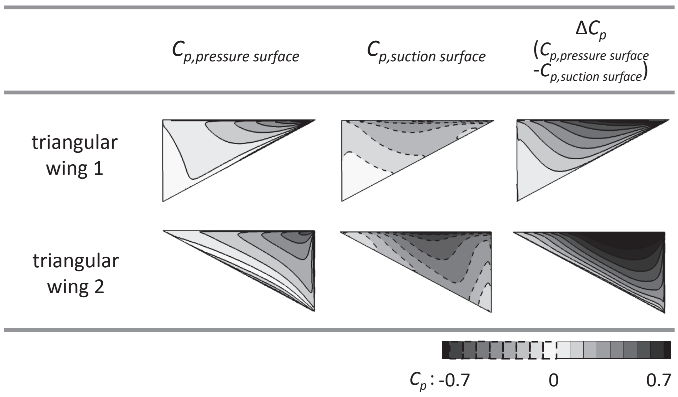

Figure 3.6. Contours of pressure coefficient (C_p) on pressure surface and suction surface of wings, and difference of pressure coefficients of triangular wings at AoA=45°, t/T =0.6; Left, right, upper, lower side of each wing is wing root, wing tip, leading edge, trailing edge, respectively. Here, solid lines indicate positive value and dashed lines indicate negative value.

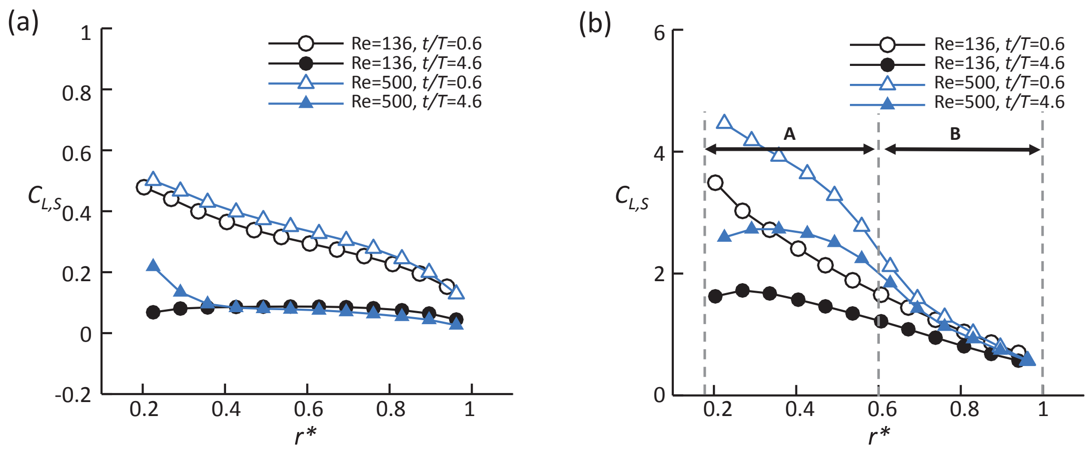

Figure 3.7. Spanwise distribution of instantaneous sectional lift coefficient at Re=136, 500 (a) AoA=5°, (b) AoA=45°.

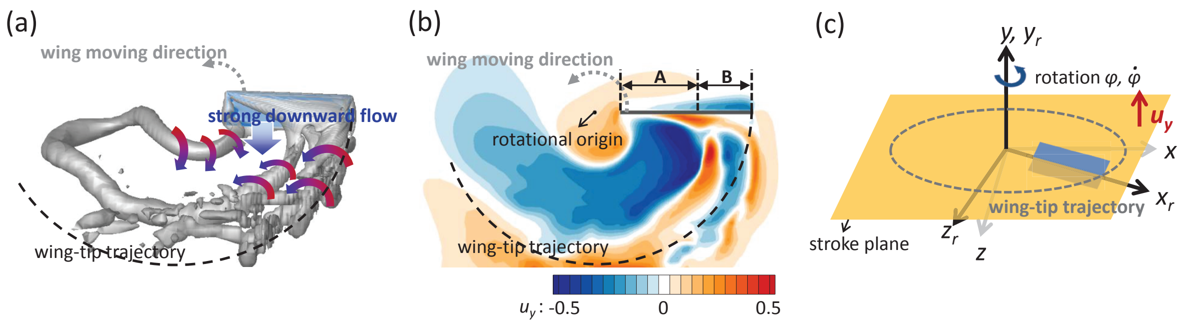

Figure 3.8. (a) Instantaneous vortical structure (λ_2 vortex definition of Jeong & Hussain (1995)) and (b) instantaneous vertical velocity (u_y) fields on the stroke plane of the wing with AoA=45° during the first rotation (t/T =0.6) at Re=500. The considered region and the definition of vertical velocity are illustrated in (c).

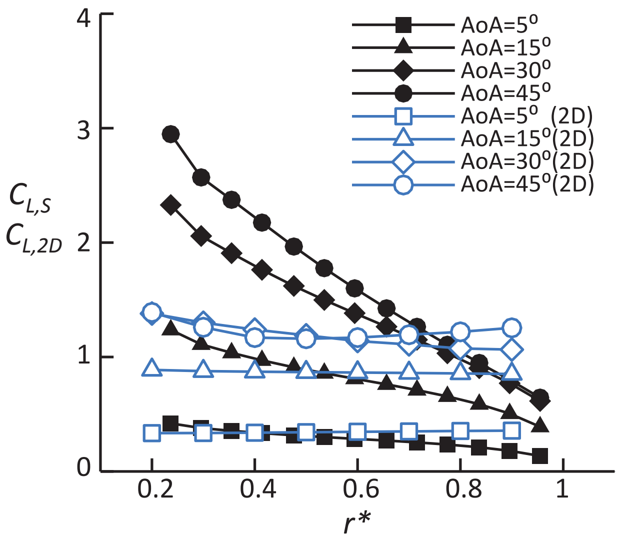

Figure 3.9. Variations of the sectional lift coefficient of 3D wing and the lift coefficient of 2D wing.

Chapter 4

Summary and Conclusions

In the present study, we conducted numerical simulations of flow around the low-aspect-ratio wing in rotating motion at low Reynolds number (Re=136) and investigated the characteristics of sectional lift coefficient ($C_{L,S}$) of the wing.

The wing started from rest and encountered the downward flow generated from previous rotation after one rotational period. After several rotations, lift force was gradually decreased influenced by downward flow lowering effective angle of attack and to be in steady state at last. The relation $C_{L,S} \sim r^n$ was obtained from instantaneous $C_{L,S}$ on the midsection of the wing at various AoAs. Interestingly, our result indicated that the sectional lift coefficient of a rotating wing was inversely proportional to the spanwise distance from the rotation center at broad range of high AoA ($40° - 80°$), and it was consistent with the previous observations.

With three different types of thin plate wings, wing shape effect on sectional lift coefficient was investigated. Although the lift coefficients of the wings showed high dependency on the wing shape, sectional lift coefficient showed similar tendency at high AoA. The behavior of sectional lift coefficient at higher Reynolds number (=500) was also investigated and it showed similar tendency at low angle of attack exhibiting slight discrepancies.

References

Birch, J.M. & Dickinson, M.H. 2001 Spanwise flow and the attachment of the leading-edge vortex on insect wings. *Nature* **412**, 729–733.

Birch, J.M. and Dickson, W.B. & Dickinson, M.H. 2004 Force production and flow structure of the leading edge vortex on flapping wings at high and low Reynolds numbers. *J. Exp. Biology* **41**, 213.

Caradonna, F.X. & Tung, C. 1981 Experimental and analytical studies of a model helicopter rotor in hover. *NASA Technical Memorandum* , 8123.

DeVoria, A.C., P. Mahajan & Ringuette, M.J. 2011 Vortex formation and saturation for low-aspect-ratio rotating flat plates at low Reynolds number. *49th AIAA Aerospace Sciences Meeting*.

Dickinson, M.H., Lehmann, F.O. & Sane, S.P. 1999 Wing rotation and the aerodynamic basis of insect flight. *Science* **284**, 1954–1960.

Jeong, J. & Hussain, F. 1995 On the identification of a vortex. *J. Fluid Mechanics* **285**, 69–94.

Kim, D. & Choi, H. 2006 Immersed boundary method for flow around an arbitrarily moving body. *J. Comput. Phys.* **212**, 662.

Kim, J., Kim, D. & Choi, H. 2001 An immersed-boundary finite-volume method for simulations of flow in complex geometries. *J. Comput. Phys.* **171**, 132.

Kim, D. & Gharib, M. 2010 Experimental study of three-dimensional vortex structures in translating and rotating plates. *Exp. Fluids* **49**, 329–339.

Kweon, J. & Choi, H. 2010 Sectional lift coefficient of a flapping wing in hovering motion. *Phys. Fluids* **22**, 071703.

Lan, SL & Sun, M. 2001 Aerodynamic properties of a wing performing unsteady rotational motions at low Reynolds number. *Acta mechanica* **149**, 135–147.

Lentink, D., Dickson, W.B., van Leeuwen, J.L. & Dickinson, M.H. 2009 Leading-edge vortices elevate lift of autorotating plant seeds. *Science* **324**, 1438.

Lentink, D. & Dickinson, M.H. 2009 Rotational accelerations stabilize leading edge vortices on revolving fly wings. *J. Exp. Biology* **212**, 2705–2719.

Luo, G. & Sun, M. 2005 The effects of corrugation and wing planform on the aerodynamic force production of sweeping model insect wings. *Acta Mech. Sin.* **21**, 531.

Morino, L., Bharadvaj, B.K., Freedman, M.I. & Tseng, K. 1989 Boundary integral equation for wave equation for wave equation with moving boundary and applications to compressible potential aerodynamics of airplanes and helicopters. *Computational Mechanics* **4**, 231–243.

Nagai, H. & Hayase, T. 2009 Experimental and numerical study of forward flight aerodynamics of insect flapping wing. *AIAA J.* **47**, 730–742.

Ozen, CA & Rockwell, D. 2012 Flow structure on a rotating plate. *Exp. Fluids*, 1–17.

Poelma, C., Dickson, W.B. & Dickinson, M.H. 2006 Time-resolved reconstruction of the full velocity field around a dynamically-scaled flapping wing. *Exp. Fluids* **41**, 213.

Sun, M. & Wu, J. 2004 Large aerodynamic forces on a sweeping wing at low Reynolds number. *Acta Mech. Sin.* **20**, 24–31.

낮은 레이놀즈 수에서 회전하는 날개의 단면 양력 계수

서울대학교 대학원
기계항공공학부
김지은

요약

본 연구에서는 3 차원 수치해석을 통해 낮은 레이놀즈 수에서 회전하는 날개의 단면 양력 계수의 특성을 살펴보았다. 날개의 평균 코드 길이와 날개 끝 속도를 기준으로 한 레이놀즈 수는 136 이며, 초파리 날개와 같은 가로세로비 (3.74) 를 갖는 각기 다른 모양(초파리 날개 형상, 사각형, 삼각형)의 평판이 정지상태에서 회전을 시작하여 일정한 받음각과 각속도를 가지고 회전하도록 하여 여러 가지 받음각에 대해 연구를 수행하였다. 첫 회전에서 날개의 단면 양력 계수의 분포는 날개의 회전 중심에서 날개 끝으로 갈수록 감소하는 경향을 보였고, 여러 바퀴를 회전하면서 이전 회전에 의해 발생한 아래 방향 유동의 영향을 받아 단면 양력 계수가 전체적으로 감소하여 평형상태에 이르게 됨을 관찰하였다. 특히 높은 받음각 (40°-80°) 을 갖는 회전 날개의 단면 양력 계수는 회전 중심으로부터 거리에 반비례 하는 특성을 보였다. 또한 높은 받음각 (45°) 에서 회전 날개의 단면 양력 계수의 분포는 날개 모양에 거의 영향을 받지 않음을 확인하였다. 3 차원 날개의 단면 양력 계수를 2 차원 수치해석 결과를 이용하여 구할 경우, 실제의 값과는 다른 값을 예측하게 되는 것으로 나타났다.

주요어: 단면 양력 계수, 회전 날개, 낮은 가로세로비 날개, 날개 모양

학번: 2011-22885